

Sensorless Direct Flux Vector Control of Synchronous Reluctance Motors Including Standstill, MTPA and Flux Weakening

Original

Sensorless Direct Flux Vector Control of Synchronous Reluctance Motors Including Standstill, MTPA and Flux Weakening / Yousefi-Talouki, Arzhang; Pescetto, Paolo; Pellegrino, Gianmario. - In: IEEE TRANSACTIONS ON INDUSTRY APPLICATIONS. - ISSN 0093-9994. - (2017), pp. 1-1. [10.1109/TIA.2017.2679689]

Availability:

This version is available at: 11583/2666788 since: 2018-02-19T15:24:58Z

Publisher:

IEEE

Published

DOI:10.1109/TIA.2017.2679689

Terms of use:

This article is made available under terms and conditions as specified in the corresponding bibliographic description in the repository

Publisher copyright

(Article begins on next page)

Sensorless Direct Flux Vector Control of Synchronous Reluctance Motors Including Standstill, MTPA and Flux Weakening

Arzhang Yousefi-Talouki, Paolo Pescetto, and Gianmario Pellegrino, *Senior Member, IEEE*

Abstract -- This paper proposes a sensorless direct flux vector control scheme for synchronous reluctance motor drives. Torque is controlled at constant switching frequency, via the closed loop regulation of the stator flux linkage vector and of the current component in quadrature with it, using the stator flux oriented reference frame. A hybrid flux and position observer combines back-electromotive force integration with pulsating voltage injection around zero speed. Around zero speed, the position observer takes advantage of injected pulsating voltage. Instead of the commonly used current demodulation, the position error feedback is extracted here at the output of the observer's flux maps, thus resulting in immunity towards the cross-saturation position error. The Maximum Torque per Ampere (MTPA) strategy is used. A detailed analysis puts in evidence the key advantages and disadvantages related to the use of the MTPA in the sensorless control of the Synchronous Reluctance machine, for both the saliency based and the back-EMF based sensorless methods. Extensive experimental results are reported for a 2.2-kW synchronous reluctance motor prototype, showing the feasibility of the proposed method. These include speed response to step and sinusoidal load disturbances at standstill, up to 121% of rated torque, and speed response tests covering the flux weakening speed region.

Index Terms--Direct flux vector control; Sensorless control; Synchronous reluctance motor; Zero speed sensorless control; Cross-saturation.

I. INTRODUCTION

In recent years, synchronous reluctance motors (SyRMs) have been widely adopted due to their low manufacturing cost and simple structure, without windings nor magnets on their rotors, and for their good efficiency [1-4]. The application of SyRMs will presumably grow in the coming years, because of the price uncertainty of rare earth raw materials used in permanent magnets, and because of stricter regulations on motors' efficiency [5]. A key condition towards a wider application of the SyRM in a large number of industrial applications is that the existing sensorless techniques are improved in terms of both performance and ease of calibration.

The direct torque control (DTC) method possesses several advantages respect to conventional current vector control, such as fast torque response and robust implementation [6-8]. The DTC is inherently a sensorless control scheme. Electromagnetic torque and stator flux amplitude are closed-loop controlled in the stator reference frame, without requiring

the rotor position feedback. However, at low speed levels, the back-electromotive force (EMF) flux estimation deteriorates and more refined flux and position observer schemes are needed for zero speed sensorless control [8]. The direct flux vector control (DFVC) method presented in [9-11] maintains the main features of DTC as well as features of vector control method such as fixed switching frequency and straightforward limitation of the current vector amplitude. In DFVC, the amplitude of the stator flux linkage and the torque current component are controlled in the stator flux synchronous frame called $d_s q_s$. Thanks to the direct control of the stator flux linkage, voltage utilization in the flux weakening speed operating region is straightforward. Similarly, the inverter current limit is explicitly handled via direct saturation of the q_s -axis current control. Both voltage and current limit blocks are parameter independent.

Two categories of sensorless methods are considered here: the ones based on back-EMF induced by rotor movement [12] and the ones using the injection of high frequency (HF) signals to track the magnetic saliency of the rotor [13]. The performance of the former ones is good above a minimum level of fundamental frequency that can be as small as 1 Hz according to the literature. Being the motional back-EMF zero at zero speed, when zero and low speed control under load are needed, the position observer is augmented with HF signal injection and demodulation. The literature reports examples of sensorless DTC of internal permanent magnet (IPM) synchronous motors using such approach [8, 14-15].

Dealing with the SyRM, this is inherently salient and complies well with signal injection-based estimation techniques. A sensorless DTC technique for PM-assisted SyRMs was proposed in [16]. In [17] a hybrid active flux-high frequency injection method was proposed for sensorless control of axially laminated SyRM drives. In [18] a back-EMF based position observer combined with high-frequency signal injection was proposed for SyRM drives. In [19], a hybrid active-flux and arbitrary signal injection for SyRMs was proposed. The transition from the active-flux and signal injection modes was handled via a speed commanded hysteresis switch. Reference [20] proposed a position sensorless vector control for transverse laminated SyR motor drives. In addition, [21] proposed a position sensorless control of SyR motors using HF current injection. However, all such

A. Yousefi-Talouki, P. Pescetto, and G. Pellegrino are with the Politecnico di Torino, Department of Energy, Corso Duca degli Abruzzi 24, 10129, Torino, Italy.

email: arzhang.yousefitalouki@polito.it, paolo.pescetto@polito.it, gianmario.pellegrino@polito.it

methods use a constant level of excitation (constant d -axis current, i.e. constant flux amplitude) instead of taking advantage of the MTPA control law. The constant excitation limits the machine's parameters variation with the load torque and guarantees an appropriate level of back-EMF signal also at zero torque, where the MTPA would command zero excitation.

To the best author's knowledge, there are only a few papers reporting the combination of the DFVC method with sensorless applications. In [22], a sensorless DFVC method was proposed for induction motors, but not at low speeds and standstill. In this paper [23], sensorless DFVC is proposed for Synchronous Reluctance Motor drives. The main contributions of this paper are:

- 1) the wide speed range sensorless algorithm, covering zero speed and flux weakening, and inherently insensitive to cross-saturation position error;
- 2) The use of MTPA in sensorless SyRM control and the analysis of the critical stability area at low excitation values;
- 3) The analysis of the machine saliency in the dq plane, addressing the critical aspects of saliency tracking via HF injection and demodulation. This analysis demonstrates that the MTPA law is also recommendable for the sake of stability of saliency based sensorless methods.

II. BACKGROUND

A. Synchronous Reluctance Motor Model

The spatial vector reference frames adopted in the paper are introduced in Fig.1: (α, β) , (d, q) and (d_s, q_s) stand for stationary frame, rotor frame and stator flux frame, respectively. The voltage equation of the SyRM in the dq frame is (1):

$$\bar{v}_{dq} = R_s \bar{i}_{dq} + \frac{d\bar{\lambda}_{dq}}{dt} + j\omega \bar{\lambda}_{dq} \quad (1)$$

Where R_s is the stator resistance, ω is the rotor angular frequency, \bar{v}_{dq} is the stator voltage vector expressed in complex form, \bar{i}_{dq} is the stator current vector, and $\bar{\lambda}_{dq}$ is the stator flux linkage vector. The electromagnetic torque is expressed as (2), where p is the number of pole pairs.

$$T = \frac{3}{2} \cdot p \cdot (\lambda_d i_q - \lambda_q i_d) \quad (2)$$

The magnetic model (3) accounts for the effects of

saturation and cross-saturation and will be stored in two 2-D flux maps (λ_d and λ_q).

$$\begin{cases} \lambda_d = \lambda_d(i_d, i_q) = L_d(i_d, i_q) \cdot i_d \\ \lambda_q = \lambda_q(i_d, i_q) = L_q(i_d, i_q) \cdot i_q \end{cases} \quad (3)$$

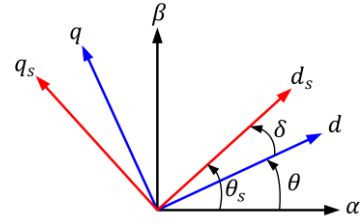


Fig. 1. Reference frames: stator (α, β) , rotor (d, q) and stator flux (d_s, q_s) coordinates.

B. Direct Flux Vector Control

Equations (4) and (5) are obtained by transferring the (1) and (2) to the stator flux reference frame (d_s, q_s) :

$$\begin{cases} v_{d_s} = R_s \cdot i_{d_s} + \frac{d\lambda}{dt} \\ v_{q_s} = R_s \cdot i_{q_s} + \lambda \cdot (\omega + \frac{d\delta}{dt}) \end{cases} \quad (4)$$

$$T = \frac{3}{2} p \cdot \frac{L_d - L_q}{2L_d L_q} \cdot \lambda^2 \cdot \sin(2\delta) \quad (5)$$

Where δ is the load angle and λ is the amplitude of the stator flux linkage vector and $\lambda_d = \lambda \cdot \cos(\delta)$, $\lambda_q = \lambda \cdot \sin(\delta)$. Alternatively, torque is expressed as:

$$T = \frac{3}{2} \cdot p \cdot \lambda \cdot i_{q_s} \quad (6)$$

From (4) it can be concluded that the stator flux amplitude λ can be regulated via the d_s - voltage component and that the load angle and consequently torque (5) could be regulated by means of the q_s -axis stator voltage. Instead, torque is controlled via closed loop control of the quadrature current component i_{q_s} , after torque equation (6). Details can be found in [9].

The block diagram of direct flux vector control scheme is illustrated in Fig.2. Gain k shown in red rectangle is a switch to turn on or off the HF injection as will be explained in section III.C. Flux amplitude λ is regulated through a first PI regulator. The closed loop bandwidth equals the proportional gain K_{p-ds} [rad/s].

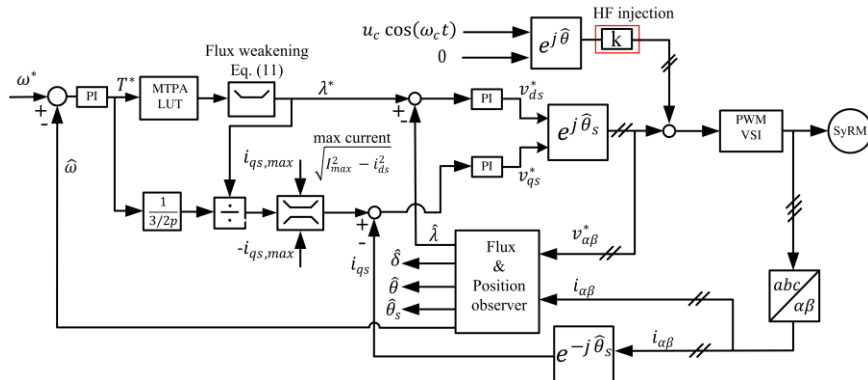


Fig. 2. Sensorless direct flux vector control scheme.

About the dynamics of i_{qs} , equation (7) is obtained equalizing (5) and (6). Equation (8) follows from (4):

$$i_{qs} = \lambda \cdot \frac{L_d - L_q}{2L_d L_q} \cdot \sin(2\delta) \quad (7)$$

$$\frac{di_{qs}}{dt} = a \cdot (v_{ds} - R_s \cdot i_{ds}) + b \cdot (v_{qs} - R_s \cdot i_{qs} - \omega\lambda) \quad (8)$$

$$a = \frac{L_d - L_q}{2L_d L_q} \cdot \sin(2\delta), \quad b = \frac{L_d - L_q}{L_d L_q} \cdot \cos(2\delta) \quad (9)$$

Equations (8)-(9) show that i_{qs} can be closed-loop controlled using the v_{qs} voltage component, with disturbances coming from the v_{ds} component controlling the flux, from the resistive voltage and the motional back-EMF $\omega\lambda$. All such effects can be either compensated or have minor impact on torque dynamics [9]. Going to the tuning of the q_s -axis PI regulator, the gain b of the plant in (9) tells that the bandwidth of PI regulator on q_s -axis will be a function of the machine operating points, i.e. will vary with L_d , L_q and δ that is, in turn, with λ and δ .

C. Stator flux observer

The stator flux observer represented in Fig.3 is one key building block of the proposed control scheme. The amplitude and phase angle of the stator flux are the outputs of the flux observer. This is based on the back-EMF integral (voltage model), plus a compensation signal built as the difference between the voltage model flux estimate and the current model flux estimate $\hat{\lambda}_{\alpha\beta,i}$ (flux maps output). The subscript i stands for ‘‘current model’’ estimate. The transfer function of the flux observer is as (10), where s is the Laplace variable and the scalar gain g (radians per second) is the crossover angular frequency between the voltage model and the current model flux estimates.

$$\hat{\lambda}_{\alpha\beta} = \frac{s}{s+g} \left(\frac{v_{\alpha\beta}^* - R_s \cdot i_{\alpha\beta}}{s} \right) + \frac{g}{s+g} \hat{\lambda}_{\alpha\beta,i} \quad (10)$$

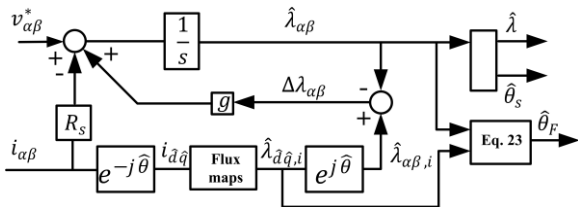


Fig. 3. Stator flux observer.

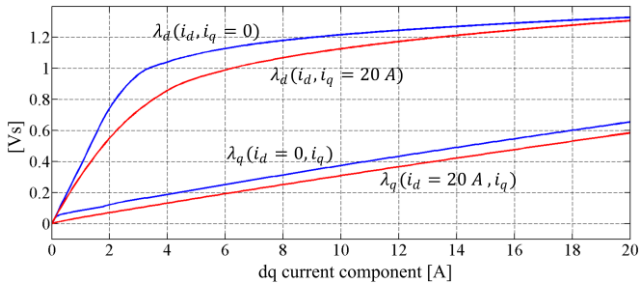


Fig. 4. Flux linkage maps of the SyRM under test, evaluated experimentally.

Equation (10) suggests that when $|\omega| > g$ voltage integration prevails, while the current model prevails for $|\omega| < g$. The motor parameters are concentrated in the ‘‘Flux maps’’ block. Fig.4 shows the flux curves of the motor studied in this

paper, representative of the flux maps block. Other motor data is in Table I.

TABLE I - SyR Machine under test specifications

SyR motor under test	
Rated power/Number of poles	2.2 kW / 4
Nominal Speed/Rated Torque	1500 r/min / 14 Nm
Nominal Phase Current (RMS)	5.1 [A]
Nominal Line-Line Voltage (RMS)	400 [V]
Phase resistance	3.5 Ω
Moment of inertia	0.005 $kg \cdot m^2$

D. Lower Limited MTPA Flux Reference

Torque and flux amplitude set points are correlated according to the MTPA law for the sake of copper loss minimization and therefore minimizing loss at low load. The MTPA torque to flux correlation is shown in Fig.5. Zero torque corresponds to zero flux amplitude. However, the zero flux situation would cancel the machine back-EMF and harm flux and position estimations. Therefore, a minimum excitation flux must be guaranteed for the sake of back-EMF tracking also around zero torque. The minimum excitation level is set here to 0.7 [Vs], highlighted in red in Fig. 5: the flux reference follows the MTPA, and it is lower saturated to 0.7 [Vs]. Section IV will show that the minimum flux level is also necessary to guarantee a minimum level of saliency in zero torque conditions, so that the HF injection method can operate correctly. The flux lower limit guarantees rotor position tracking over the whole speed operating range.

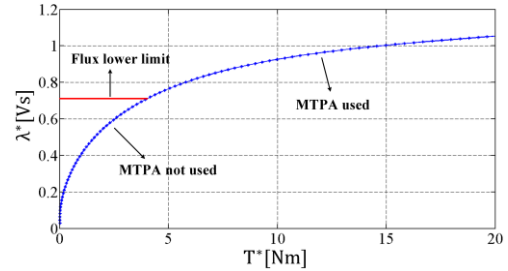


Fig. 5. Flux reference amplitude according to the MTPA law.

E. Flux Weakening and Current Limitation

The inverter voltage limit is respected by reducing the flux reference as (11), where v_{dc} is measured dc-link voltage and $V_{max} \cong v_{dc}/\sqrt{3}$.

$$\lambda^* \leq \frac{[V_{max} - R_s \cdot i_{qs} \cdot \text{sign}(\hat{\omega})]}{|\hat{\omega}|} \quad (11)$$

It is not necessary to know the corner speed a priori: the block (11) adapts the flux reference according to the actual speed and the available voltage. Current amplitude is limited to the maximum converter value (I_{max}) by limiting the q_s -axis current reference (12).

$$i_{qs}^* \leq \sqrt{(I_{max}^2 - i_{ds}^2)} \quad (12)$$

III. SENSORLESS CONTROL SCHEME

This section describes the sensorless control method proposed in this paper. The observer gain g is set to 35 [rad/s]. Equation (10) suggests that the current and voltage models are

combined according to the angular frequency ω and the observer gain g . Given the pole-pair number $p = 2$, 35 electrical rad/s corresponds to 167 r/min. Therefore, the region [0~50] r/min is where flux estimation is predominantly based on the current model, the range [50-500] r/min is where both current and voltage models heavily contribute to flux estimate and 500 r/min and over is where the back-EMF integration model is predominant. The high frequency signal injection is progressively dropped out between 50 r/min and 100 r/min. It is well-known that high frequency injection should be turned off as soon as possible to remove related noise and additional loss, and to comply with the converter voltage limit.

A. High-Frequency Signal Injection Method

A pulsating voltage component (50 V peak, 833 Hz) is superimposed to the voltage reference signal on the estimated \hat{d} -axis direction. Fig.6 shows the estimated reference frame (\hat{d}, \hat{q}), aligned with the estimated rotor position $\hat{\theta}$. The position estimation error is named $\Delta\theta$. u_c is the amplitude of the injected pulsating voltage and ω_c is the carrier frequency.

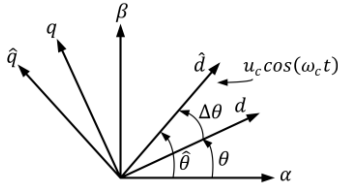


Fig. 6. Actual and estimated rotor reference frames.

Conventionally, the \hat{q} -axis current component is demodulated and imposed to be zero by way of a rotor position tracking loop [18]. The current response to the high-frequency voltage, expressed in \hat{d} and \hat{q} components is as (13), where B , L_{cm} , and L_{dm} are as (14). L_{dd} and L_{qq} are the self-axis incremental inductances and L_{dq} is the mutual inductance.

$$\begin{cases} I_{\hat{d}HF} = B \cdot [L_{cm} - L_{dm} \cos(2\Delta\theta) - L_{dq} \sin(2\Delta\theta)] \\ I_{\hat{q}HF} = B \cdot [L_{dm} \sin(2\Delta\theta) - L_{dq} \cos(2\Delta\theta)] \end{cases} \quad (13)$$

$$\begin{cases} B(i_d, i_q) = \frac{u_c \sin(\omega_c t)}{\omega_c (L_{dd} L_{qq} - L_{dq}^2)} \\ L_{cm} = \frac{L_{dd} + L_{qq}}{2}, L_{dm} = \frac{L_{dd} - L_{qq}}{2} \end{cases} \quad (14)$$

The position information contained in the signal $I_{\hat{q}HF}$ is prone to the effect of cross-saturation, due to the term $L_{dq} \cos(2\Delta\theta)$ in (13). This causes a position estimation error, which is also variable with the operating conditions as it is the term $L_{dq}(i_d, i_q)$. Such error can be model compensated as suggested in [18],[24]. Conversely, in this paper the high-frequency response of the motor on the \hat{q} direction is evaluated downstream the flux map in the observer, as depicted in Fig. 7, rather than upstream. In turn, the current response (13) is multiplied by the flux maps of the motor, and the \hat{q} component of the obtained output signal (15) is demodulated and used for position tracking. This inherently overcomes the cross-

saturation error effect. The HF component of the flux maps output is:

$$\begin{bmatrix} \hat{\lambda}_{\hat{d}HF,i} \\ \hat{\lambda}_{\hat{q}HF,i} \end{bmatrix} = \begin{bmatrix} L_{dd} & L_{dq} \\ L_{dq} & L_{qq} \end{bmatrix} \begin{bmatrix} I_{\hat{d}HF} \\ I_{\hat{q}HF} \end{bmatrix} \quad (15)$$

Where the subscript HF indicates the high-frequency component of the flux maps output defined in Fig. 3.¹ Manipulating (13) and (15), the position feedback signal $\hat{\lambda}_{\hat{q}HF,i}$ (16) is obtained.

$$\hat{\lambda}_{\hat{q}HF,i} = B \cdot \{L_{dq} L_{cm} [1 - \cos(2\Delta\theta)] + [L_{qq} L_{dm} - L_{dq}^2] \sin(2\Delta\theta)\} \quad (16)$$

Differently from $I_{\hat{q}HF}$, the signal (16) is zero when $\Delta\theta$ is zero (**no position error caused by L_{dq}**). If $\Delta\theta$ is small, the term $[1 - \cos(2\Delta\theta)]$ in (16) can be neglected. Therefore, (16) can be approximated as (17).

$$\hat{\lambda}_{\hat{q}HF,i} \cong B \cdot [L_{qq} L_{dm} - L_{dq}^2] \sin(2\Delta\theta) \quad (17)$$

Considering the above mathematics, it is seen from Fig. 7 that the $\hat{\lambda}_{\hat{q}HF,i}$ signal comes from the $\hat{\lambda}_{\hat{q},i}$ component of Fig. 3 after band-pass filtering. Then, $\hat{\lambda}_{\hat{q}HF,i}$ is demodulated and low pass filtered to obtain the error signal (ϵ). φ_d is for compensation of discretization delay coming from digital implementation.

$$\epsilon = LPF[\hat{\lambda}_{\hat{q}HF,i} \cdot \sin(\omega_c t)] \quad (18)$$

This is proportional to the position estimation error, as turns out after manipulation of (14), (17)-(18):

$$\epsilon = \frac{u_c}{2\omega_c} \cdot \frac{L_{qq} L_{dm} - L_{dq}^2}{L_{dd} L_{qq} - L_{dq}^2} \cdot \sin(2\Delta\theta) \quad (19)$$

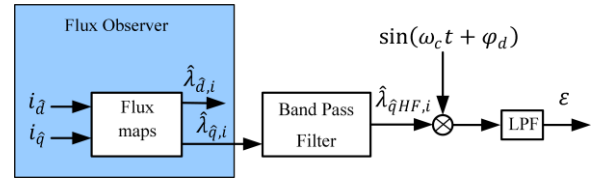


Fig. 7. HF-injection-based demodulation process.

Fig.8 illustrates the tracking loop used for rotor position estimation. The error signal (19) is the source of a PI regulator that forces the position error to zero. Around $\Delta\theta = 0$, equation (19) can be written as (20), where k_ϵ is as (21).

$$\epsilon \cong k_\epsilon \cdot \Delta\theta \quad (20)$$

$$k_\epsilon = \frac{u_c}{\omega_c} \cdot \frac{L_{qq} L_{dm} - L_{dq}^2}{L_{dd} L_{qq} - L_{dq}^2} \quad (21)$$

Equations (16) and subsequent shows that the position error signal is not affected by the cross-saturation effect: if the pulsating voltage is aligned correctly ($\Delta\theta = 0$), then the position error signal is also zero.

¹ In case of non-zero position error, the signals (15) do not represent the flux estimate coming from the current model in the \hat{d}, \hat{q} coordinates. This is true only when the estimated position is tracked correctly ($\Delta\theta = 0, \hat{d} \equiv d$).

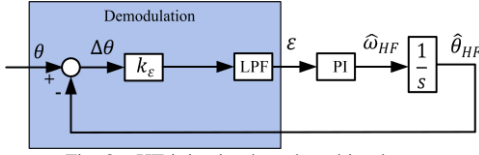


Fig. 8. HF-injection based tracking loop.

B. Tuning of the Tracking Loop

The closed-loop bandwidth of the position tracking loop $\omega_{bw, HF}$ is conventionally set to be three-times lower than the cutoff frequency of the low pass filter ($f_{LPF} = 50$ Hz here) [18].

$$\omega_{bw, HF} = k_\epsilon \cdot k_{p, HF} < \frac{1}{3} \cdot 2\pi \cdot f_{LPF} \quad (22)$$

$k_{p, HF}$ in (22) is the proportional gain of the PI regulator.

The closed loop bandwidth depends from the error gain factor k_ϵ , which is dependent from the motor operating point. Fig.9 shows the values of k_ϵ for different working points of the motor under test. As can be seen from this figure, the critical area is around $i_q = 0$ (i.e. zero torque), where the error signal gain tends to vanish and even to become negative, when i_d is not zero (i.e. for non-zero excitation flux). If k_ϵ is zero or negative, the position tracking fails.

Dealing with the proposed control technique, the red line in Fig.9 represents the minimum guaranteed excitation flux 0.7 [Vs], whilst the blue line corresponds to the MTPA law. In turn, the lower bounded MTPA control strategy guarantees that k_ϵ is always positive, including the no load area, and its value spans from a minimum of 0.002 [Vs] to a maximum of 0.004 [Vs]. Therefore, the PLL operation is always stable and the position estimation bandwidth varies in a range from one to two, with constant PI parameters, according to (22).

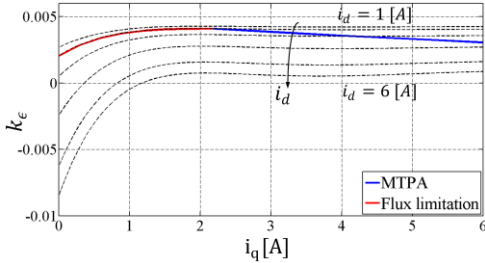


Fig. 9. Different values of k_ϵ as a function of i_q and i_d .

C. Hybrid Flux and Position Observer Scheme

The rotor position and speed estimates coming from the back-EMF model are expressed in (23) and (24), respectively. The subscript ‘‘F’’ denotes that position and speed come from flux estimation and f_s is sampling frequency.

$$\begin{cases} \sin(\hat{\theta}_F) = \frac{\hat{\lambda}_{d,i} \cdot \hat{\lambda}_\beta - \hat{\lambda}_{q,i} \cdot \hat{\lambda}_\alpha}{|\hat{\lambda}_i| |\hat{\lambda}|} \\ \cos(\hat{\theta}_F) = \frac{\hat{\lambda}_{d,i} \cdot \hat{\lambda}_\alpha + \hat{\lambda}_{q,i} \cdot \hat{\lambda}_\beta}{|\hat{\lambda}_i| |\hat{\lambda}|} \end{cases} \quad (23)$$

$$\hat{\omega}_{F,k} = (\sin \hat{\theta}_{F,k} \cos \hat{\theta}_{F,k-1} - \cos \hat{\theta}_{F,k} \sin \hat{\theta}_{F,k-1}) \cdot f_s \quad (24)$$

Position estimation (23) is combined with the HF-injection contribution through the smooth fusion scheme reported in Fig.10. The gain k is responsible of progressively switching on and off the injected voltage signal (Fig. 2) and the PI output

contribution to the rotor position estimate (Fig. 10). Below 50 [r/min], k is equal to 1. Between 50 and 100 [r/min] k decreases progressively from 1 to 0. Above 100 [r/min] the PI output and the pulsating voltage injection itself are dropped out completely. The feedback gain (h) in Fig. 10 helps the smooth transition between the two position estimation schemes, with and without the k branch.

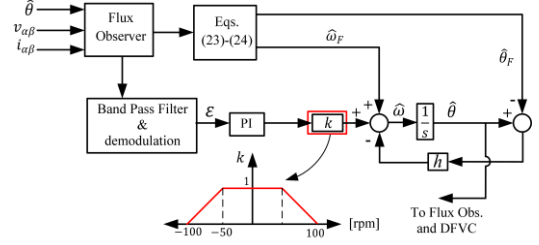


Fig. 10. Proposed combined rotor position observer.

D. Bode Analysis of the two Position Estimates Fusion

The position observer of Fig.10 combines the HF-injection based tracking loop (Fig. 8) with the position estimation coming from the back-EMF (23). After manipulation, the estimated rotor position ($\hat{\theta}$) is obtained as (25).

$$\begin{cases} \hat{\theta} = G_{HF} \cdot \theta + G_F \cdot \hat{\theta}_F \\ G_{HF} = \frac{H}{H+1} \\ G_F = \frac{1}{H+1} \end{cases} \quad (25)$$

G_{HF} and G_F are the transfer functions of the HF-injection and the back-EMF based position estimates θ and $\hat{\theta}_F$, respectively. In (25), H is the open loop transfer function of the HF-injection based tracking loop:

$$H = \frac{1}{1 + \frac{2\pi f_{LPF}}{s}} \cdot \frac{k_\epsilon k_{i, HF} + s k_\epsilon k_{p, HF}}{s} \cdot k \cdot \frac{1}{s+h} \quad (26)$$

The Bode diagram of the two transfer functions G_{HF} and G_F of (25) is reported in Fig.11, referring to the case $k = 1$ (< 50 r/min, HF-injection activated). The PI gains are set to $k_{p, HF} = 30.000$, $k_{i, HF} = 125.000$. The gain h has been set 25 [rad/s]. As can be seen, the two transfer functions are one low-pass and one high-pass filters, with a common cutoff frequency at 17 [Hz]. This corresponds to the crossover of H , and it is three times smaller than the LPF cutoff frequency by design. Although the HF injection is on, the information coming from back-EMF position estimation (G_F component) is yet covering the high frequency range of the frequency response, i.e., in occasion of mechanical transients.

In the speed area between 50 and 100 [r/min] k decreases progressively to zero, shifting down the open-loop $|H|$ diagram, and shifting backwards the crossover between the HF and F models. As an example, Fig.12 shows the Bode diagrams at 85 [r/min], when $k = 0.3$. At this speed, the bandwidth of the tracking loop is approximately 7 [Hz].

When the speed goes beyond 100 [r/min], the HF injection is dropped out completely. With $k = 0$, the crossover frequency is equal to zero, the G_{HF} disappears from the diagram and G_F diagram is equal to 0 dB in the whole frequency range. The position estimation is now purely based on $\hat{\theta}_F$.

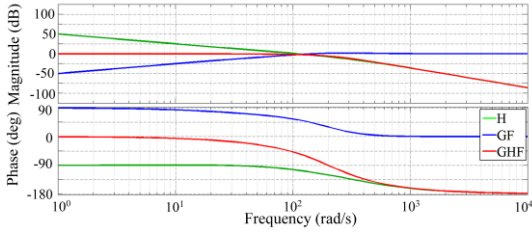


Fig. 11. Bode diagram of (25) and (26) when $k = 1$ (< 50 r/min)

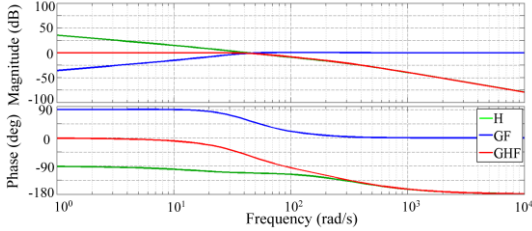


Fig. 12. Bode diagram of (25) and (26) when $k = 0.3$ (85 r/min)

IV. SALIENCY ANALYSIS OF THE SYRM

This section analyzes the machine saliency as a function of the i_d, i_q operating point, with the aim of evaluating the critical issues related to cross saturation and possible loss of control in the zero torque and zero excitation areas, when using HF voltage injection and saliency information.

Although the saliency characteristics of interior PM machines have been thoroughly studied in [25], the SyRM has specific issues, in particular when i_q is close to zero, that is around zero torque also for the DFVC. In these conditions, the incremental inductance of the q axis tends to be very similar to the one of the d axis, leading to lack of saliency and lack of position information. This phenomenon can be noticed from the curves $\lambda_d(i_d, i_q = 0)$ and $\lambda_q(i_d = 0, i_q)$ in Fig. 4, having similar slope around zero current. This has to do with the saturation of the structural ribs in the rotor: if i_q is too small, the bridges conduct flux linearly and the machine is quasi isotropic. Interior PM and PM-assisted SyR machines do not suffer from such zero current saliency issue, since in those cases the PM flux is strong enough to saturate the bridges also at zero current. Another characteristic of SyRM is that cross-saturation is usually more relevant than in PM machines, and this is also affecting the saliency.

A. Saliency Evaluation through Rotating Excitation

The current response to a rotating HF voltage signal is used to explore the saliency of the SyRM over the i_d, i_q operational plane. Fig. 13a reports the incremental current response in the i_d, i_q current plane of the machine under test. Given any operational point i_d, i_q , the superposition of a rotating voltage excitation produces an elliptic current response, superimposed to the average operating point. The main direction of the ellipse indicates the direction with the lowest incremental inductance. Assuming no cross saturation ($L_{dq} = 0$), the incremental current responses along the d and q axes (peak values) are:

$$\Delta i_d \cong \frac{u_c}{\omega_c L_{dd}}, \quad \Delta i_q \cong \frac{u_c}{\omega_c L_{qq}} \quad (27)$$

In normal circumstances, $L_{dd} \gg L_{qq}$ produces a sharp current ellipse oriented along the q axis, and the rotor position is tracked with no error. This is true in the left hand side of Fig. 13a, within the MTPA trajectory bound. In other points, to the right side of the MTPA, the ellipse is deviated and deformed by the cross-saturation effect, leading to a position estimation error and even to the loss of position tracking. The chart of Fig. 13a was obtained by manipulation of a fine mesh flux map evaluated with finite element analysis (FEA). The rotating voltage has an amplitude of 50 V (same as for the alternated voltage used for the sensorless DFVC) and the current ellipse deformation and deviation from the vertical axis puts in evidence the cross saturation effects.

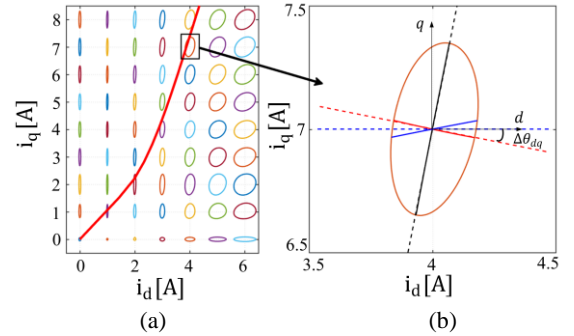


Fig. 13. a) Current response to a 50V rotating voltage injection. MTPA in red; b) Comparison between pulsating and rotating injection for a working point on the MTPA. FEM model has been used.

B. Pulsating Injection and Ellipse Deviation

The cross-saturation position error is (28), either with rotating or pulsating voltage injection [24]:

$$\Delta \theta_{dq} = \frac{1}{2} \arctg \left(\frac{2L_{dq}}{L_{dd} - L_{qq}} \right) \quad (28)$$

Fig. 13b compares the current responses of pulsating and rotating injections for one point of the MTPA trajectory. A pulsating voltage of 50 V is injected in three different directions, indicated by the dashed lines. The continuous lines represent the computed path of the pulsating current, accounting for the effect of cross saturation. The results of Fig. 13b are summarized here:

- The blue lines are when the HF voltage is injected along the correct d axis, and the obtained current deviates from the injection direction.
- Red lines: the blue lines tell what happens with open loop voltage injection along the d axis. If the current component on the estimated q axis is used as input of a position tracking loop, the blue situation would produce a position error that the tracking loop would correct, converging in the steady state situation $\hat{\theta} = \Delta \theta_{dq}$, where the HF current and voltage are aligned (red).
- Black test: a position observer might also converge at $\hat{\theta} = \Delta \theta_{dq} + \frac{\pi}{2}$ (black), for symmetry reasons.

Altogether, Fig. 13b shows that the current ellipse summarizes the information coming from all possible injection directions, when using a pulsating signal. Moreover, the position error is easy to visualize as the deviation between the ellipse minor axis and the horizontal directions. This is why

rotating excitation has been used in this section. FEA and experimental results are compared in Fig. 14.

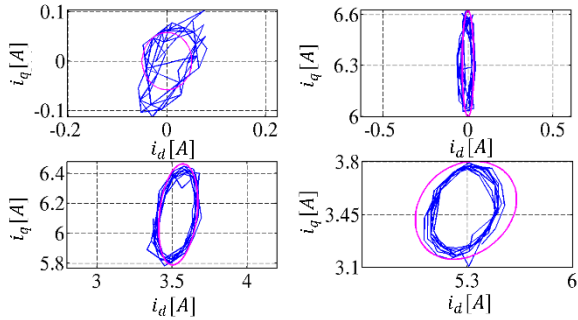


Fig. 14. Comparison between FEM model (magenta) and experimental measurements (blue) for rotating voltage injection. Upper: origin (left) and q -axes (right); Lower: points on the MTPA (left) and in the unstable region (right).

C. Stability Region and Zero Current

As said, the position error is negligible where the ellipse is sharp and vertical, i.e. left wise respect to the MTPA curve. Conversely, in the right end side of Fig. 13a the position error becomes significant, and in the lower right corner (around the d axis) the saliency even reverses (sharp horizontal ellipses), indicating that the position tracking error could be equal to 90° . Moreover, a special case of lack of position information is in the origin where the saliency is very low, for the mentioned ribs effect. This is confirmed in Fig. 14, where the current trajectory resembles a circle rather than an ellipse. Besides the origin, the d -axis region altogether ($i_q \cong 0$) tends to be critical for saliency, for the combination of the non-saturated ribs and the direct saturation due to the d -axis component. The ellipses on the d -axis in Fig. 13a indicate that saliency can reverse ($L_{dd} < L_{qq}$).

The stable region of saliency based sensorless methods is summarized in Fig. 15, in green. The unstable region is indicated in brown, covering those points where the cross saturation error (28) is larger than 45° and the saliency tracking would converge 90° away from the d -axis. Also, the unfeasible region includes the origin of the plane, where there is no saliency and position tracking fails.

D. Selection of the Minimum Excitation Flux

The vertical magenta line in Fig. 15 stands for the 0.7 Vs locus of minimum excitation of the DFVC, introduced in section II. In this machine, 0.7 Vs fairly coincides with $i_d = 2A$. This is the flux reference value that the DFVC uses for zero and very low torque values, as said. The value 0.7 Vs was selected so that the magenta line can fall inside the green area of stability of Fig. 15. If a lower flux value was chosen (e.g. $i_d < 2A$) this would have shifted the vertical line colored in magenta closer to the instability area in the origin of the plane. Similarly, if a higher value of flux was chosen, the magenta line might have fallen into the instability region to the right end side of the plane.

Moreover, having a non-zero minimum flux is advantageous also for model based flux and position estimate. The value 0.7 Vs guarantees a minimum signal value to back-EMF estimation and tracking.

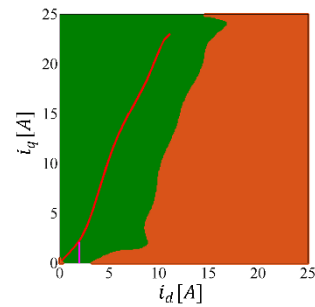


Fig. 15. Stable (green) and unstable (brown) regions at zero and low speed. Red: MTPA. Magenta: minimum flux limit.

V. EXPERIMENTAL RESULTS

This section presents and discusses the experimental results for the proposed control strategy. The data for the SyRM under test is reported in Table I. The sampling and switching period is $T_s = 100 \mu s$. A quadrature encoder with 512 cycles per revolution is used for position and speed monitoring purposes. A variable speed load drive (ABB Selivector) is used to impose the load torque or set the speed in the different experiments. The experimental setup is represented in Fig.16, equipped with a dSPACE 1103 PPC controller board. Also, inverter specifications are tabulated in Table II.

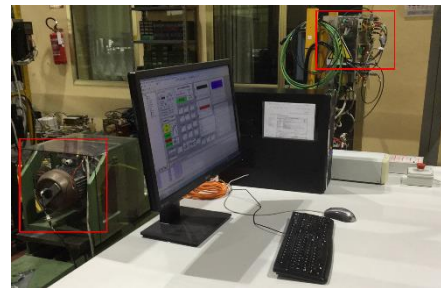


Fig. 16. Experimental test bench: The dSPACE 1103 PPC host computer is on the desk. The SyR motor under test is in the red square to the left. Power converter is in another red square in the right-hand corner.

TABLE II - Inverter specifications

IGBT PM50RVA120	
dc-link voltage	560 [V]
Dead time	3 [μs]

A. Torque Step Response

The motor is torque controlled and positive and negative step of reference torque are applied at standstill (Fig. 17) and 50 [r/min] (Fig. 18). The speed is controlled by the load drive. Figures 17 (a) and (b) show the tests results at standstill where ± 12 [Nm] torque is applied at $t = 2[s]$. It can be seen that for both positive and negative step torques, the position estimation error is close to zero. Furthermore, the performance of the drive can be observed in Fig.18, for ± 12 [Nm] step torque command when the rotor speed is kept at 50 [r/min]. Also at this speed the position estimation error is close to zero.

B. Zero Cross-Saturation Error

As proved mathematically, the demodulation process of the $\hat{\lambda}_{q,i}$ signal instead of the \hat{q} -axis current component overcomes the cross-saturation effect in HF based position estimation. This is experimentally shown in Fig.19, where a 0 to 14 [Nm] torque reference ramp is applied to the motor, with the speed set to

zero by the load drive. As seen, the position estimation error is close to zero at all torque values. The response when using a demodulation process based on \hat{q} -axis current component is shown in Fig.20. The position estimation error moves proportionally to torque, unless model based compensation is added to the position tracking process [18]. It should be noted that the torque and flux waveforms shown in Figures 19 and 20 are the observed quantities. Since these tests were performed in torque control mode, in both tests the same profiles of the references (λ^*, i_{qs}^*) were imposed and consequently the PI regulators force the feedbacks ($\hat{\lambda}, i_{qs}$) to follow the respective references. Therefore, the two tests seem to deliver the same torque, despite of the non-negligible position error in Fig. 20, but they are not. Actual torque values are different from estimated ones, and this is particularly true for the results of Fig. 20, since the position error is relevant. Torque estimate in Fig. 19 is considered correct.

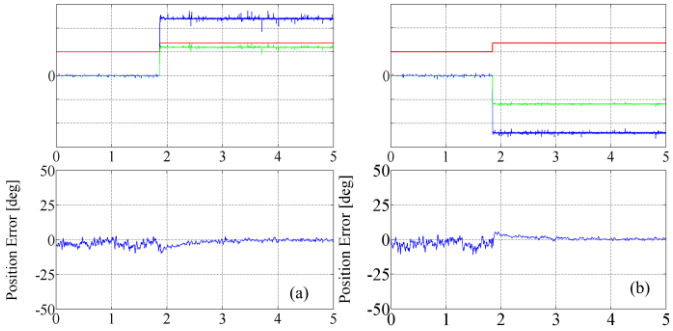


Fig. 17. Torque control at standstill with ± 12 [Nm] step torque: (a) 12 [Nm] step torque, (b) -12 [Nm] step torque. Top figures, blue: \hat{T} (5 Nm/div); green: i_{qs} (3.5 A/div); red: $\hat{\lambda}$ (0.7 Vs/div).

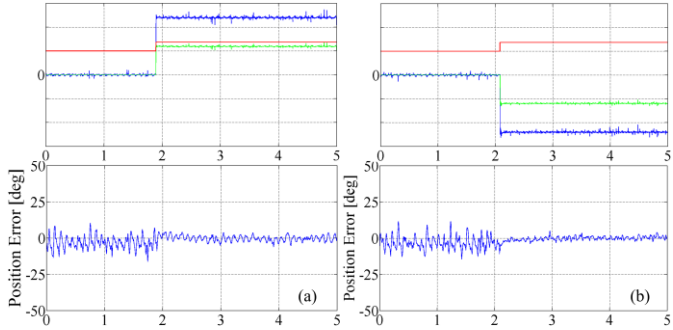


Fig. 18. Torque control at 50 [r/min] with ± 12 [Nm] step torque: (a) 12 [Nm] step torque, (b) -12 [Nm] step torque. Top figures, blue: \hat{T} (5 Nm/div); green: i_{qs} (3.5 A/div); red: $\hat{\lambda}$ (0.7 Vs/div).

C. Speed Response to Load Steps at Standstill

The motor is speed controlled at standstill under 17 [Nm] load steps (121% of full load). Results are reported in Fig.21. As can be seen, load is applied to the motor at $t = 1.5$ [s] and released at $t = 7$ [s]. The response of the system during transients and in steady state is acceptable and position estimation error is close to zero.

D. Flux Weakening

Fig. 22 reports fast ramp responses from 0 to 3000 [r/min] and then to -3000 [r/min]. As can be seen, flux kicks in around 2000 [r/min]. The position estimation error is zero in steady state and under control in transients.

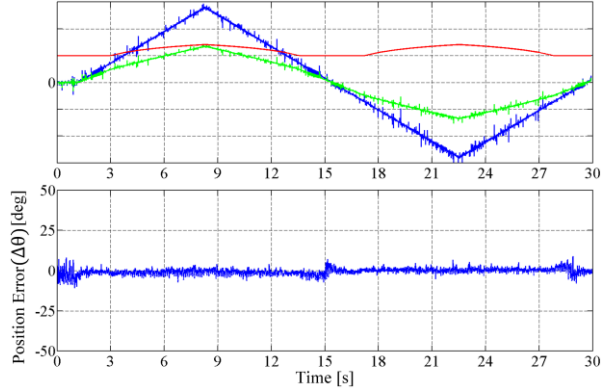


Fig. 19. Torque control at standstill with 14 [Nm] ramp load when $\hat{\lambda}_{\hat{q}_i}$ component is demodulated. Top figure, blue: \hat{T} (5 Nm/div); green: i_{qs} (3.5 A/div); red: $\hat{\lambda}$ (0.7 Vs/div).

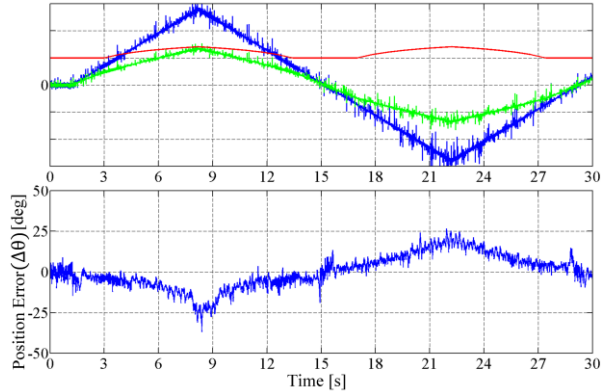


Fig. 20. Torque control at standstill with 14 [Nm] ramp load when \hat{q} -axis current component is demodulated. Top figure, blue: \hat{T} (5 Nm/div); green: i_{qs} (3.5 A/div); red: $\hat{\lambda}$ (0.7 Vs/div).

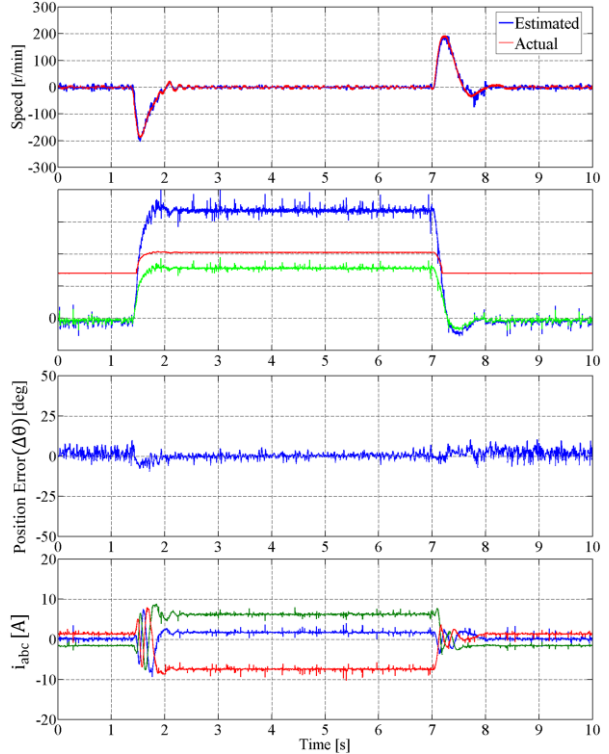


Fig. 21. Drive performance in standstill under 17 [Nm] load. Second figure from the top: blue: \hat{T} (5 Nm/div); green: i_{qs} (3.5 A/div); red: $\hat{\lambda}$ (0.5 Vs/div).

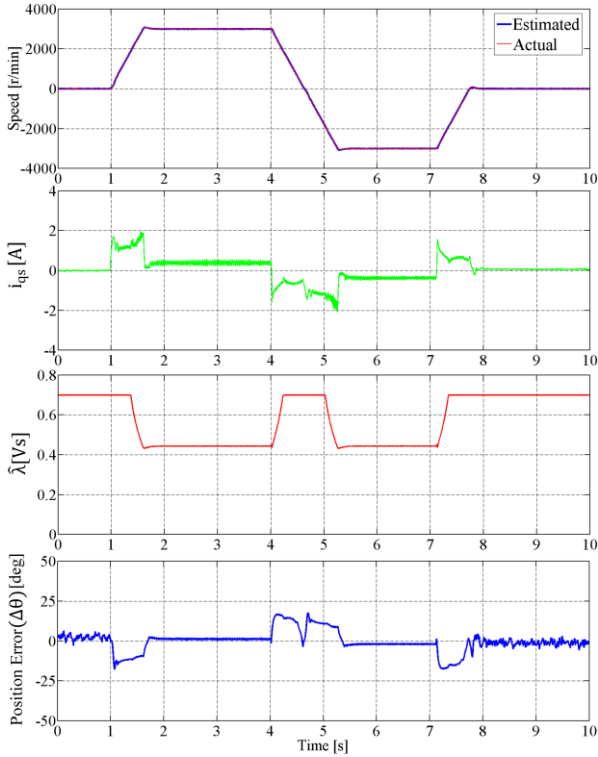


Fig. 22. Flux weakening test from 0→3000→-3000→0 [r/min].

E. Speed Response to Sinusoidal Torque Disturbances

In this section, the proposed sensorless speed control is tested by applying a sinusoidal torque disturbance having a frequency that progressively increases from 0 to 5 [Hz]. The test was performed at standstill and the sinusoidal load has an amplitude of 50% rated load, superimposed to a constant load torque equal to another 50% of nominal one. Altogether, the load torque during the test oscillates from zero to full-load.

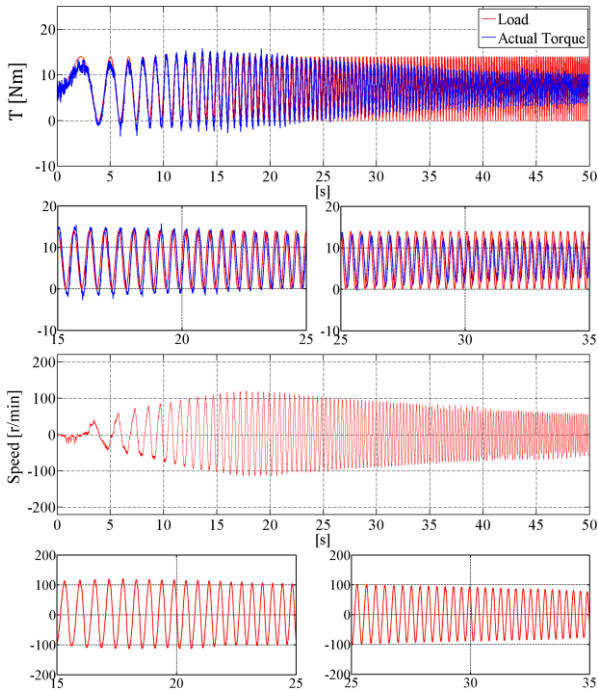


Fig. 23. Motor response to torque disturbances in DFV control with encoder.

The same test was repeated with and without the encoder (Figs. 23 and 24, respectively), with the same tuning of the PI speed regulator, for the sake of performance comparison and validation of the sensorless technique. The speed and torque response of the drive to the torque disturbances is very similar in the two cases. In Fig. 24 the observed torque follows the applied torque up to 3 [Hz] with zero position estimation error thanks to the bandwidth of the sensorless control and also the inherent compensation of the cross-saturation effect. After 3 [Hz] the amplitude of the torque response tends to vanish, due to bandwidth limitations.

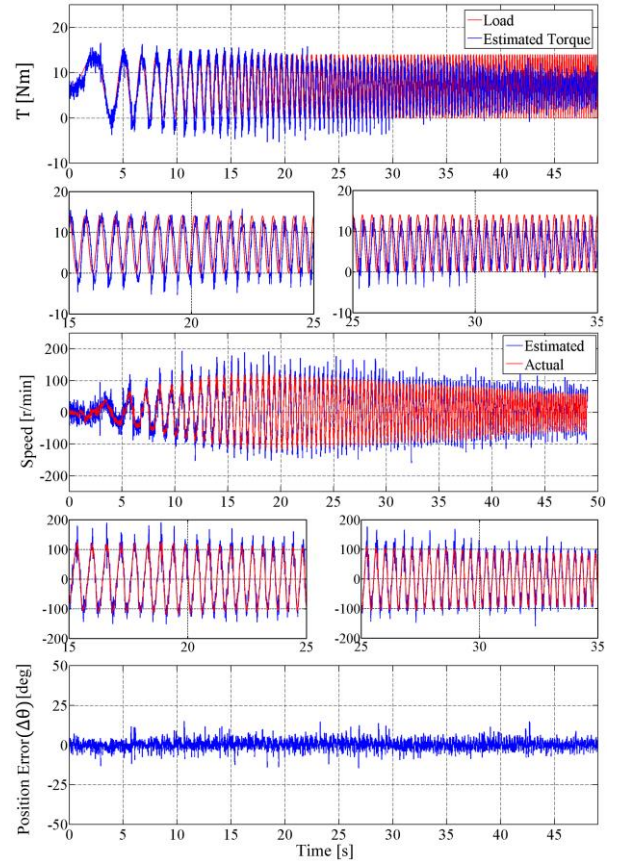


Fig. 24. Motor response to torque disturbances in sensorless DFV control.

VI. CONCLUSION

The paper presented a sensorless direct flux vector control method for synchronous reluctance motor drives. The proposed hybrid position observer is capable of covering a wide speed range including standstill and flux weakening. Pulsating voltage injection associated to proposed demodulation technique guarantees inherent immunity to cross-saturation deviation of the position estimate. The specific challenges related to the adoption of the MTPA law associated to the sensorless control of the SyRM have been addressed and extensively discussed. The MTPA related issues can affect both the back-EMF and HF injection sensorless methods, as shown in the paper. The saliency of the SyRM has been analyzed in detail, to put in evidence the singularity of the zero excitation point, and to demonstrate that the MTPA is also a key region of stability for saliency based sensorless methods. The proposed control scheme was successfully validated

through various experimental tests. The reported results show the good performance of the drive both at steady state and during transients.

VII. REFERENCES

[1] Vagati, A.; Pastorelli, M.; Franceschini, G., "High-performance control of synchronous reluctance motors," *Industry Applications, IEEE Transactions on*, vol.33, no.4, pp.983,991, Jul/Aug 1997.

[2] Boglietti, A.; Cavagnino, A.; Pastorelli, M.; Vagati, A., "Experimental comparison of induction and synchronous reluctance motors performance," *Industry Applications Conference, 2005. Fourtieth IAS Annual Meeting. Conference Record of the 2005*, vol.1, no., pp.474,479 Vol. 1, 2-6 Oct. 2005.

[3] Bon-Ho Bae; Seung-Ki Sul, "A novel dynamic overmodulation strategy for fast torque control of high-saliency-ratio AC motor," in *Industry Applications, IEEE Transactions on*, vol.41, no.4, pp.1013-1019, July-Aug. 2005.

[4] Xinan Zhang; Foo, G.H.B.; Vilathgamuwa, D.M.; Maskell, D.L., "An Improved Robust Field-Weakening Algorithm for Direct-Torque-Controlled Synchronous-Reluctance-Motor Drives," in *Industrial Electronics, IEEE Transactions on*, vol.62, no.5, pp.3255-3264, May 2015.

[5] "Rotating Electrical Machines—Part 30-1: Efficiency Classes of line operated AC motors" (IE-Code), Ed. 1, IEC 60034-30-1, Dec. 2014.

[6] Zhong, L.; Rahman, M.F.; Hu, W.Y.; Lim, K.W., "Analysis of direct torque control in permanent magnet synchronous motor drives," in *Power Electronics, IEEE Transactions on*, vol.12, no.3, pp.528-536, May 1997.

[7] Inoue, Y.; Morimoto, S.; Sanada, M., "Comparative Study of PMSM Drive Systems Based on Current Control and Direct Torque Control in Flux-Weakening Control Region," in *Industry Applications, IEEE Transactions on*, vol.48, no.6, pp.2382-2389, Nov.-Dec. 2012.

[8] Foo, G.; Sayeef, S.; Rahman, M.F., "Low-Speed and Standstill Operation of a Sensorless Direct Torque and Flux Controlled IPM Synchronous Motor Drive," in *Energy Conversion, IEEE Transactions on*, vol.25, no.1, pp.25-33, March 2010.

[9] Pellegrino, G.; Bojoi, R.I.; Guglielmi, P., "Unified Direct-Flux Vector Control for AC Motor Drives," in *Industry Applications, IEEE Transactions on*, vol.47, no.5, pp.2093-2102, Sept.-Oct. 2011.

[10] Pellegrino, G.; Armando, E.; Guglielmi, P., "Direct-Flux Vector Control of IPM Motor Drives in the Maximum Torque Per Voltage Speed Range," in *Industrial Electronics, IEEE Transactions on*, vol.59, no.10, pp.3780-3788, Oct. 2012.

[11] Pellegrino, G.; Boazzo, B.; Jahns, T.M., "Plug-in Direct-Flux Vector Control of PM Synchronous Machine Drives," in *Industry Applications, IEEE Transactions on*, vol.51, no.5, pp.3848-3857, Sept.-Oct. 2015.

[12] Foo, G.H.B.; Rahman, M.F., "Direct Torque Control of an IPM-Synchronous Motor Drive at Very Low Speed Using a Sliding-Mode Stator Flux Observer," in *Power Electronics, IEEE Transactions on*, vol.25, no.4, pp.933-942, April 2010.

[13] J. M. Liu and Z. Q. Zhu, "Novel Sensorless Control Strategy With Injection of High-Frequency Pulsating Carrier Signal Into Stationary Reference Frame," in *IEEE Transactions on Industry Applications*, vol. 50, no. 4, pp. 2574-2583, July-Aug. 2014.

[14] Andreescu, G.; Pitic, C.I.; Blaabjerg, F.; Boldea, I., "Combined Flux Observer With Signal Injection Enhancement for Wide Speed Range Sensorless Direct Torque Control of IPMSM Drives," in *Energy Conversion, IEEE Transactions on*, vol.23, no.2, pp.393-402, June 2008.

[15] D. Nguyen, R. Dutta, M. F. Rahman and J. E. Fletcher, "Performance of a Sensorless Controlled Concentrated-Wound Interior Permanent-Magnet Synchronous Machine at Low and Zero Speed," in *IEEE Transactions on Industrial Electronics*, vol. 63, no. 4, pp. 2016-2026, April 2016.

[16] I. Boldea *et al.*, "DTFC-SVM motion-sensorless control of a PM-assisted reluctance synchronous machine as starter-alternator for hybrid electric vehicles," in *IEEE Transactions on Power Electronics*, vol. 21, no. 3, pp. 711-719, May 2006.

[17] Agarlita, S.-C.; Boldea, I.; Blaabjerg, F., "High-Frequency-Injection-Assisted "Active-Flux"-Based Sensorless Vector Control of Reluctance

Synchronous Motors, With Experiments From Zero Speed," in *Industry Applications, IEEE Transactions on*, vol.48, no.6, pp.1931-1939, Nov.-Dec. 2012.

[18] Tuovinen, T.; Hinkkanen, M., "Adaptive Full-Order Observer With High-Frequency Signal Injection for Synchronous Reluctance Motor Drives," in *Emerging and Selected Topics in Power Electronics, IEEE Journal of*, vol.2, no.2, pp.181-189, June 2014.

[19] Barnard, F.J.W.; Villet, W.T.; Kamper, M.J., "Hybrid Active-Flux and Arbitrary Injection Position Sensorless Control of Reluctance Synchronous Machines," in *Industry Applications, IEEE Transactions on*, vol.51, no.5, pp.3899-3906, Sept.-Oct. 2015.

[20] E. Capecchi, P. Guglielmi, M. Pastorelli and A. Vagati, "Position-sensorless control of the transverse-laminated synchronous reluctance motor," in *IEEE Transactions on Industry Applications*, vol. 37, no. 6, pp. 1768-1776, Nov.-Dec. 2001.

[21] Seog-Joo Kang, Jang-Mok Kim and Seung-Ki Sul, "Position sensorless control of synchronous reluctance motor using high frequency current injection," in *IEEE Transactions on Energy Conversion*, vol. 14, no. 4, pp. 1271-1275, Dec 1999.

[22] Bojoi, R.; Guglielmi, P.; Pellegrino, G., "Sensorless Stator Field-Oriented Control for Low Cost Induction Motor Drives with Wide Field Weakening Range," in *Industry Applications Society Annual Meeting, 2008. IAS '08. IEEE*, vol., no., pp.1-7, 5-9 Oct. 2008.

[23] A. Yousefi-Talouki and G. Pellegrino, "Sensorless direct flux vector control of synchronous reluctance motor drives in a wide speed range including standstill," *2016 XXII International Conference on Electrical Machines (ICEM)*, Lausanne, 2016, pp. 1167-1173.

[24] Guglielmi, P.; Pastorelli, M.; Vagati, A., "Impact of cross-saturation in sensorless control of transverse-laminated synchronous reluctance motors," in *Industrial Electronics, IEEE Transactions on*, vol.53, no.2, pp.429-439, April 2006.

[25] N. Bianchi and S. Bolognani, "Influence of Rotor Geometry of an IPM Motor on Sensorless Control Feasibility," in *IEEE Transactions on Industry Applications*, vol. 43, no. 1, pp. 87-96, Jan.-feb. 2007.



Arzhang Yousefi-Talouki received the Bachelor degree in electrical engineering from University of Mazandaran, Iran in 2009, and the Master degree from Babol University of Technology, Babol, Iran in 2012. He is currently working toward the PhD degree in Politecnico di Torino, Turin, Italy. His current research interests include electrical machine drives, especially synchronous motor drives and sensorless control.



Paolo Pescetto is a PhD student at the Politecnico di Torino, Turin, Italy. He received the Bachelor and Master degree in the same university in 2013 and 2015, respectively, with full grade and honours in both cases. In 2014 he has been an Erasmus+ student at the Norwegian University of Science and Technology. His current research interests include synchronous motor drives, sensorless control and self-commissioning techniques.



Gianmario Pellegrino, (M'06-SM'13) received the M.Sc. and Ph.D. degrees in electrical engineering from the Politecnico di Torino, Turin, Italy, in 1998 and 2002, respectively. He is currently an Associate Professor with the same university. His research interests include the design of electrical machines and the control of electrical drives. He is involved in research projects with industry and has 30 journal papers and one patent. Dr. Pellegrino is an Associate

Editor for the *IEEE Transactions on Industry Applications*. He is the co-recipient of six Prize Paper Awards. He was a visiting scholar at Aalborg University, Denmark, at the University of Nottingham, UK and at the University of Wisconsin-Madison, USA.